Poly(ethylene oxide) Crystal Orientation Changes in an Inverse Hexagonal Cylindrical Phase Morphology Constructed by a Poly(ethylene oxide)-*block*-polystyrene Diblock Copolymer

Ping Huang,[†] Joseph X. Zheng,[†] Siwei Leng,[†] Ryan M. Van Horn,[†] Kwang-Un Jeong,[†] Ya Guo,[†] Roderic P. Quirk,[†] Stephen Z. D. Cheng,*[,†] Bernard Lotz,[‡] Edwin L. Thomas,[§] and Benjamin S. Hsiao[⊥]

Maurice Morton Institute and Department of Polymer Science, The University of Akron, Akron, Ohio 44325-3909; Institute Charles Sadron, 6 Rue Boussingault, Strasbourg 67083, France; Department of Materials Science and Engineering, Massachusetts Institute of Technology, Cambridge, Massachusetts 02139; and Department of Chemistry, State University of New York at Stony Brook, Stony Brook, New York 11794-3400

Received August 14, 2006; Revised Manuscript Received October 23, 2006

ABSTRACT: A poly(ethylene oxide)-*block*-polystyrene (PEO-*b*-PS) diblock copolymer with number-average molecular weights of 7.7k g/mol for the PS block and 21.4k g/mol for the PEO block was used to study the PEO crystal orientation changes at different crystallization temperatures (T_x) via small- and wide-angle X-ray scattering techniques. For this diblock copolymer, an inverse hexagonal cylinder (IHC) phase morphology was identified with PS cylinders hexagonally packed within the PEO matrix. In this IHC morphology, the PEO blocks were tethered on the convex interfaces of the PS domains, and the crystallization of PEO blocks was outside of the cylinders. The crystal orientation of the PEO blocks (the *c*-axis of the PEO crystals) after crystallization among the PS cylinders was, for the first time, found to change with respect to the long cylinder axis, $\hat{a}$, depending solely on T_x. At very low T_x's, when the samples were quenched into liquid nitrogen, the crystals possessed a random orientation. When $-30\ ^\circ\text{C} \le T_x \le 5\ ^\circ\text{C}$, PEO crystals had an orientation with their *c*-axis parallel to $\hat{a}$. Within the temperature region of $10\ ^\circ\text{C} \le T_x \le 20\ ^\circ\text{C}$, the *c*-axis crystal orientation changed to be tilted with respect to $\hat{a}$ (the tilting angle was defined to be between the *c*-axis of the PEO crystals and $\hat{a}$). This tilting angle increased with increasing T_x. Finally, a major crystal orientation with the *c*-axes of PEO crystals perpendicular to $\hat{a}$ was observed when T_x reached 30 °C. Furthermore, it was particularly interesting that the PEO crystals in the IHC phase were oriented in two dimensions when $T_x = 30\ ^\circ\text{C}$. Namely, the PEO crystal growth was specifically grown along the $\{10\bar{1}0\}$ planes of the hexagonal PS cylinders. The crystallite sizes were estimated by the Scherrer equation. The PEO crystal sizes, at least along one dimension, were on the scale of the sizes limited by the distance between the neighboring glassy PS cylinders in the hexagonal lattice.

Introduction

Crystalline−amorphous diblock copolymers can be used to construct nanoconfined environments of lamellae, double gyroids, cylinders, or spheres based on the block compositions. The crystal structure, orientation, and crystallization kinetics of different kinds of semicrystalline blocks in diblock copolymers, such as polyethylene (PE),[1−17] poly(ethylene oxide) (PEO),[18−32] poly(L-lactic acid),[33−35] poly(ϵ-caprolactone),[36−38] and poly(tetrahydrofuran) (PTHF),[39−41] within those confined environments, have been extensively investigated. Since the strong phase separation takes place between two blocks when the temperature is below the order−disorder transition temperature (T_{ODT}) and since the glass transition temperature (T_g) of the amorphous blocks in these systems is higher than the melting temperature (T_m) of the crystalline blocks, hard nanoconfinements can be achieved.[24] When the T_g is slightly lower than the T_m in a crystalline−amorphous diblock copolymer, the amorphous blocks may form a soft-confined environment for the crystalline blocks.[24] The degree of softness of this confinement is dependent on the difference between the T_g and the T_m and the speed of the crystallization kinetics. The "breakout" crystallization may also be observed when the amorphous confinements are very soft.[10,11,15,16,22,25,42−48]

Among those studies about confined crystallization and crystal orientation changes within the nanoenvironments constructed using block copolymers, almost all of them have focused on the systems which possess a continuous amorphous phase (except for the lamellar phase) in order to generate the solid matrix in the nanoconfined environments. The systems in which the crystalline blocks form a continuous phase—crystallization of a matrix in an inverse phase morphology—have only been investigated by a few groups.[13,14,41,49] So far, two publications have appeared in the studies of the crystal orientation in the inverse hexagonal cylinder (IHC) phase. In the first publication, a polystyrene-*block*-(polyethylene-*alt*-propylene)-*block*-PE (PS-*b*-PEP-*b*-PE) triblock copolymer was used.[13] It was observed that the *b*- and *c*-axes of the PE crystals were predominantly parallel and perpendicular to the long axis of the PS cylinders ($\hat{a}$), respectively. In the second study, an unusual 2D-preferred orientation of the PE crystals within the matrix of the IHC phase constructed by PS-*b*-PE and poly(vinyl cyclohexane)-*block*-PE (PVCH-*b*-PE) diblock copolymers was reported.[14] The PE crystals tended to grow with their *b*-axes parallel to $\hat{a}$, while in the plane normal to $\hat{a}$, the PE crystals tend to align their *c*-axes parallel to the $\{10\bar{1}0\}$ planes of the hexagonal macrolattice. In addition, Liu et al. studied the blend of poly(methyl methacryl-

* To whom correspondence should be addressed. E-mail: scheng@uakron.edu.
[†] The University of Akron.
[‡] Institute Charles Sadron.
[§] Massachusetts Institute of Technology.
[⊥] State University of New York at Stony Brook.

10.1021/ma061871h CCC: $37.00
Published on Web 01/12/2007

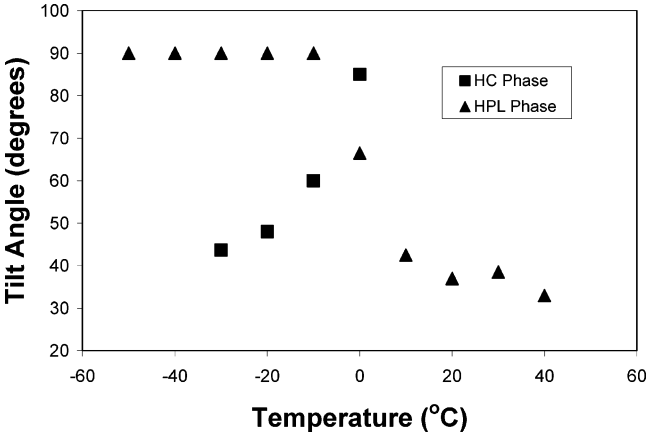

Figure 1. Relationships between the tilt angle and crystallization temperature for both the HC phase and the HPL phase.[26−28,32] The tilt angle is defined as an angle between the *c*-axes of the PEO crystals and the cylinder long axis $\hat{a}$ (note that in the HPL phase, the $\hat{a}$ direction is parallel to the lamellar normal).

ate)-*block*-PTHF and PTHF homopolymer with an IHC phase. They proposed crystallite morphologies and packing models in the IHC system; yet, no experimental observations of the crystal orientation were detailed.[41] So far, to our best knowledge, no crystal orientation changes with crystallization temperature (T_x) in the IHC phases have been reported.

In this study, we report the crystal orientation change with T_x in an IHC phase constructed by a PEO-*b*-PS diblock copolymer. This investigation is closely associated with two of our previous studies in PEO-*b*-PS copolymers: one is the PEO block crystallization within confined cylinders constructed by an HC phase morphology,[26,32] and another is confined crystallization of PEO blocks in a hexagonal perforated layer (HPL) phase morphology.[27,28] For the IHC morphology the amorphous PS blocks form hexagonally packed cylinders within the matrix of the PEO blocks. In contrast to the previous studies, the crystal will be outside of the cylinders with convex glass walls in the IHC phase. On the other hand, the crystallizable PEO blocks are nanoseparated as a discontinuous phase in the HPL phase, while in the IHC phase, the PEO blocks are a macroscopically continuous matrix. This leads to a substantial difference of the crystallization behavior of the PEO blocks.

On the basis of our previous studies,[26,32] the *c*-axis orientation of the PEO crystals within the cylinders of the HC phase were found to change from random, to tilt, and to perpendicular with respect to $\hat{a}$ as T_x increases. No parallel orientation of the *c*-axes with respect to $\hat{a}$ could be found. In the case of the confined HPL phase constructed by a PEO-*b*-PS diblock, the *c*-axis orientation of the PEO crystals changed from random, to perpendicular, and to tilt with respect to the layer normal axis as T_x increases. No parallel orientation of the *c*-axis with respect to the layer normal could be found. In the HPL phase, the PEO blocks are tethered on both the layer and perforated cylinder surfaces, while in the IHC phase, the PEO blocks are only tethered on the cylinder surfaces. If we define a tilt angle between the *c*-axes of the PEO crystals and the cylinder long axis $\hat{a}$ (note that in the HPL phase the $\hat{a}$ direction is parallel to the lamellar normal axis), both relationships between the tilt angles and T_x can be plotted for the HC phase and the HPL phase nanoconfinements, as shown in Figure 1.[26−28,32]

In order to study the PEO block crystallization and crystal orientation behaviors among the PS cylinders in the IHC phase, we have synthesized a PEO-*b*-PS diblock copolymer with M_n^{PEO} = 21.4K g/mol and M_n^{PS} = 7.7K g/mol. The T_m^{PEO} is ∼62 °C.

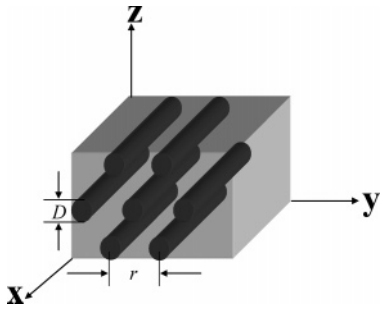

Figure 2. Geometry of the mechanically sheared PEO-*b*-PS copolymers with an inverse hexagonal cylindrical phase morphology.

The T_g^{PS} cannot be clearly discerned by differential scanning calorimetry (DSC) due to the modest PS content and interference from the melting of the PEO crystals.[50] However, the T_g of the PS blocks in a PS-*block*-poly(dimethylsiloxane) (PS-*b*-PDMS) diblock copolymer which has M_n^{PS} of 6.3K g/mol and weight fraction of 0.29 was found to be 62 °C.[51] Our estimation of the T_g^{PS} of this PEO-*b*-PS is around 55 °C. The oriented samples were investigated using combined two-dimensional (2D) small angle and wide-angle X-ray scattering (SAXS and WAXS) techniques to monitor the PEO crystal orientation changes with T_x in the confined IHC phase.

Experimental Section

Materials and Sample Preparation. The PEO-*b*-PS diblock copolymer was synthesized via sequential anionic block copolymerization of styrene and ethylene oxide monomers. Detailed synthesis procedures can be found elsewhere.[52] The PS precursor was characterized by size exclusion chromatography (SEC) using polystyrene standards and had an M_n^{PS} of 7.7K g/mol and a polydispersity of 1.02. The M_n^{PEO} was determined by proton nuclear magnetic resonance to be 21.4K g/mol. A polydispersity of 1.04 in the overall diblock copolymer was determined by SEC using the universal calibration. The volume fraction of PS blocks was then determined to be 0.275. The volume fraction of the PS blocks (f_{PS}) in the melt at 60 °C was calculated on the basis of densities of amorphous PEO and PS (1.092 and 1.035 g/cm^3, respectively).[24]

In order to ensure the consistency of the phase behavior, an identical sample preparation procedure was utilized. The sample was cast from a 5% (w/v) toluene solution, and the solvent was evaporated slowly under a dry nitrogen atmosphere by a gradual rise in temperature to above the T_m^{PEO} and then kept at 70 °C to prevent crystallization of the PEO blocks. Residual solvent was further removed under vacuum at 50 °C. In order to study the crystal orientation in the copolymer, the samples were subjected to a large-amplitude oscillating shear in a pair of parallel plates under dry argon to achieve parallel alignment of the IHC phase morphology. The shear frequency was 1 Hz; the shear amplitude was 200% at a shear temperature of 120 °C. The shear direction and resulting IHC phase morphology are schematically shown in Figure 2. The *x* direction is the shear direction, and the *z* direction is the shear gradient direction. The *xy* plane is the shear plane.

The sheared sample was about 3 × 5 × 0.1 mm^3. One sample was used for one set of X-ray experiments at different T_x values. In this publication, three sheared samples were independently prepared to obtain the experimental data. Their results were reproducible, and the tilt angle deviation was within ±5°.

Equipment and Experiments. Simultaneous 2D SAXS and WAXS experiments were conducted at the X27C synchrotron X-ray beamline of the National Synchrotron Light Source at Brookhaven National Laboratory. The wavelength of the X-ray beam was 0.1371 nm. The zero pixel of the 2D SAXS patterns was calibrated using silver behenate with the first-order scattering vector ($q = 4\pi \sin\theta/\lambda$, where λ is the wavelength and 2θ is the scattering angle) being 1.076 nm^{-1}. The 2D WAXS results were calibrated using α-Al_2O_3 with known 2θ crystal diffraction. Air scattering background was

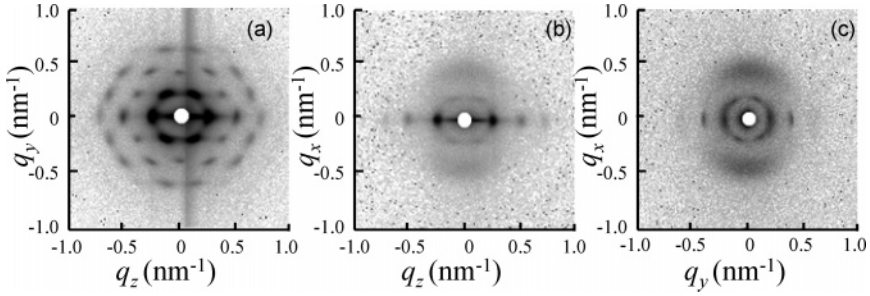

Figure 3. Set of 2D SAXS patterns of PEO-*b*-PS crystallized at −20 °C when the X-ray beam is along (a) the *x*, (b) the *y*, (c) the *z* directions.

subtracted. Azimuthal profiles were obtained from the 2D WAXS patterns by scanning 360° at a specific diffraction 2θ in an area of $2\theta \pm 0.5°$.

In order to analyze the apparent crystallite sizes of the PEO crystals formed in the IHC environment, the Scherrer equation was used:[53]

$$D_{\mathrm{hkl}} = \frac{K\lambda}{\beta_{hkl}\cos\theta} \tag{1}$$

where D_{hkl} is the apparent crystallite size along the [*hkl*] direction, *K* is the shape factor (the Scherrer constant, a value of 0.94 is used in this case), β_{hkl} is the line breadth, and θ is the half-scattering angle. Usually, β_{hkl} is taken as the half-width at half-maximum (hwhm) of an (*hkl*) diffraction. In this study, it was the (120) diffraction. Assuming that the diffraction peak shape obeyed a Gaussian function, Warren's correction can be used to correct instrument broadening:[53]

$$\frac{\beta_{hkl}}{B_{\mathrm{hkl}}} = \sqrt{1 - \frac{b^2}{B_{hkl}{}^2}} \tag{2}$$

where B_{hkl} is the experimentally observed hwhm of the diffraction peak and *b* is the hwhm of a standard specimen diffraction. To ensure a good calibration, the apparent crystallite size of the standard specimen should be >60 nm. A quartz line at 60.0° was taken for the standard *b*.

Since the PEO blocks were in the matrix and less confined as compared with systems in which the PEO blocks were in the nanoseparated phases and PS blocks were in the matrix, crystallization of the PEO blocks was fast. In order to judge how fast the cooling rates should be to obtain isothermal PEO block crystallization, we utilized a hyper-DSC accessory on the Perkin-Elmer Pyris Diamond DSC which was designed to achieve a fast and controlled cooling rate up to 500 °C/min in a temperature range between 70 and −80 °C. Liquid nitrogen was used as the coolant. Using different cooling rates between 5 and 500 °C/min, we could estimate the lowest isothermal T_x values below which the isothermal crystallization could not be carried out. Detailed experiments were done by placing the copolymer thin film samples, which were solution cast (with a weight of about 0.05 mg and a thickness of 2 μm), onto a small piece of thin flat aluminum foil (0.6 × 0.6 cm^2 with a weight of less than 0.5 mg). In this setup, the thin film samples were completely contacted with aluminum and then with the Pt/Rh sample holder which was directly connected to the oven in the DSC to minimize the thermal gradient and ensure the thermal conductivity. The samples were then heated to 70 °C and held there for 3 min before different controlled cooling rates were applied to observe the location of the exothermal crystallization peak.

Isothermal crystallization experiments on the shear-aligned samples were conducted using an Instec LN2-P2 isothermal stage equipped with a liquid nitrogen cooling system. The isothermal T_x was controlled to within an accuracy of ±0.5 °C. The samples were preheated to 70 °C for 3 min and then quickly quenched (switched) to the stage at a preset T_x for crystallization using liquid nitrogen as the coolant.

Results and Discussion

Phase Morphology of the Shear-Aligned Sample Deduced in Reciprocal Space. Figure 3 shows a set of the 2D SAXS patterns of the mechanically sheared PEO-*b*-PS sample after crystallization at −20 °C. Figure 3a is the 2D SAXS pattern when the X-ray beam is aligned along the *x* direction. In this 2D SAXS pattern, up to five orders of diffraction can be observed. They are the $(10\bar{1}0)$, $(1\bar{2}10)$, $(20\bar{2}0)$, $(21\bar{3}0)$, and $(30\bar{3}0)$ diffractions of the 2D hexagonal structure. The relationship of these diffractions is $q/q^* = 1{:}\sqrt{3}{:}2{:}\sqrt{7}{:}3$ (q^* is the first scattering vector). The 6-fold symmetry of this pattern clearly indicates that the PS cylinders in this sample are packed into a 2D hexagonal lattice. The PS long cylinder axis, $\hat{a}$, is parallel to the *x* direction (the shear direction). In this figure, a pair of the $[10\bar{1}0]$ directions are perpendicular to the shear (the *xy*) plane; therefore, the $(10\bar{1}0)$ planes of the hexagonal lattice are oriented parallel to the *xy* plane.

Parts b and c of Figure 3 are the SAXS patterns with the X-ray beam aligned to the *y* and *z* directions of the hexagonal lattice (see Figure 2), respectively. If the hexagonal lattice is perfectly oriented with the $(10\bar{1}0)$ planes parallel to the *xy* plane, only the $(10\bar{1}0)$, $(20\bar{2}0)$, and $(30\bar{3}0)$ diffractions should be observed when the X-ray is aligned with the *y* direction (in Figure 3b). Meanwhile, only the $(1\bar{2}10)$ diffraction should appear if the X-ray is aligned with the *z* direction (in Figure 3c). However, in Figure 3c the $(10\bar{1}0)$ diffraction can also be seen, indicating that the phase morphology obtained in the mechanically sheared sample is a polydomain hexagonal lattice mixture separated by grains. Moreover, weak diffraction arcs are also seen in the quadrants in Figure 3b,c, implying that the orientation of the PS cylinders within these samples is not perfect.

Quantitative analysis based on the SAXS patterns and the volume fraction of PS blocks of this copolymer shows that the distance between neighboring centers of the PS cylinders, *r*, is 29.6 nm, and each PS cylinder diameter, *D*, is 16.3 nm (see Figure 2).

Crystal Orientation Changes in Different T_x Regions. The copolymer sample was quenched into liquid nitrogen or isothermally crystallized at different T_x values using liquid nitrogen as the coolant. The T_x region was $-30\ °C \le T_x \le 30\ °C$. All the 2D SAXS patterns recorded at different T_x values after the PEO isothermal crystallization were identical to those in Figure 3a−c, indicating that the IHC phase morphology of the PS cylinders is retained in this T_x region, and hence, the PEO blocks are crystallized outside of the cylinders.

Since the PEO blocks are now the matrix, the crystallization kinetics of the PEO blocks should be much faster than those in hard confinements previously studied. For example, in a similar molecular weight range, at a cooling rate of 5 °C/min for the lamellar confined environment, the exothermic peak of the PEO block crystallization appears at 26 °C.[24] In the case of the HC confined environment, the exothermic peak of the PEO block

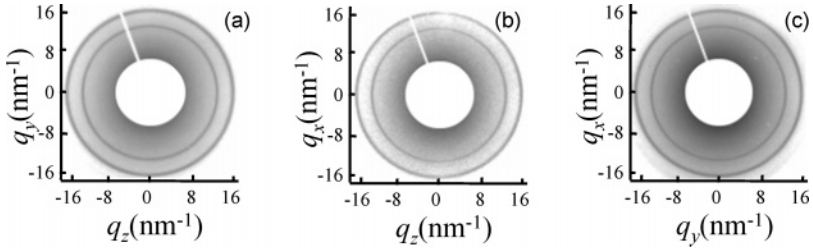

Figure 4. Set of 2D WAXS patterns of PEO-*b*-PS crystallized after being quenched into liquid nitrogen. The X-ray beam is along (a) the *x*, (b) the *y*, and (c) the *z* directions.

crystallization appears at −27 °C at a cooling rate of 10 °C/min.[32] On the other hand, for a PEO homopolymer with similar molecular weight, its exothermic crystallization peak appears above 50 °C when the cooling rate ≤10 °C/min.

Therefore, the first step to conduct this investigation is to understand at which T_x the isothermal crystallization can still be conducted. Because of the design features of the hyper-DSC, we can achieve a fast controlled cooling rate up to 500 °C/min. At a cooling rate of 40 °C/min, the exothermic peak temperature of this sample is observed at 36.6 °C; while at a cooling rate of 200 °C/min, this exothermic peak temperature shifts to 23.3 °C. If we plot a relationship between the exothermal peak temperature of the PEO crystallization and the logarithm of the cooling rate, an extrapolation leads to a temperature of −30 °C at which the exothermic peak of the PEO crystallization should appear when a cooling rate is equivalent to quenching to liquid nitrogen (2100 °C/s).[54] We thus carry out the study of isothermal crystallization kinetics of the PEO-*b*-PS sample down to a T_x of −30 °C.

Crystal Orientation When Crystallized from Quenching in Liquid Nitrogen. Parts a, b, and c of Figure 4 show a set of 2D WAXS patterns with the X-ray beams aligned along the *x*, *y*, and *z* directions, respectively, conducted on the PEO-*b*-PS sample after being quickly quenched into a liquid nitrogen slurry. In this experiment, the PEO blocks are estimated to be crystallized during quenching and/or being brought back to room temperature. All of the 2D WAXS patterns possess isotropic ring diffractions. The inner ring is attributed to the (120) diffractions (*d*-spacing of 0.463 nm), and the outer ring is the overlapped ($\bar{1}$32), (032), (112), ($\bar{2}$12), ($\bar{1}$24), ($\bar{2}$04), and (004) diffractions (overlapped *d*-spacing of 0.38−0.40 nm). It is deduced that the homogeneous nucleation density is high and that the crystal growth is not carried out far enough to complete the crystallization in such high supercoolings. Therefore, the PEO crystals are randomly oriented outside of the PS cylinders disregarding the shape and size of the environment.

Crystal Orientation When Crystallized between −30 °C ≤ T_x ≤ 5 °C. The 2D WAXS patterns, having the X-ray beam aligned along the *x*, *y*, and *z* directions for the mechanically sheared copolymer sample that is quickly quenched from 70 °C to various T_x values between −30 and 5 °C using liquid nitrogen as coolant, are shown in Figure 5a−i for three T_x values (−30, −20, and 5 °C). The WAXS patterns which were taken along the *x* direction in Figure 5a,d,g exhibit two major isotropic diffraction rings, similar to the case shown in Figure 4a. However, in the 2D WAXS patterns at these T_x values along the *y* and *z* directions, as shown in Figure 5b,c,e,f,h,i, they all exhibit a pair of the (120) diffractions located on the equator. The azimuthal scanning profiles for these (120) diffractions at these T_x values when the X-ray beam is along the *y* direction are shown in Figure 6a. This reveals that the *c*-axes of the PEO crystals are parallel to $\hat{a}$ when the T_x is between −30 and 5 °C. On the basis of these analyses, a real space model for the PEO

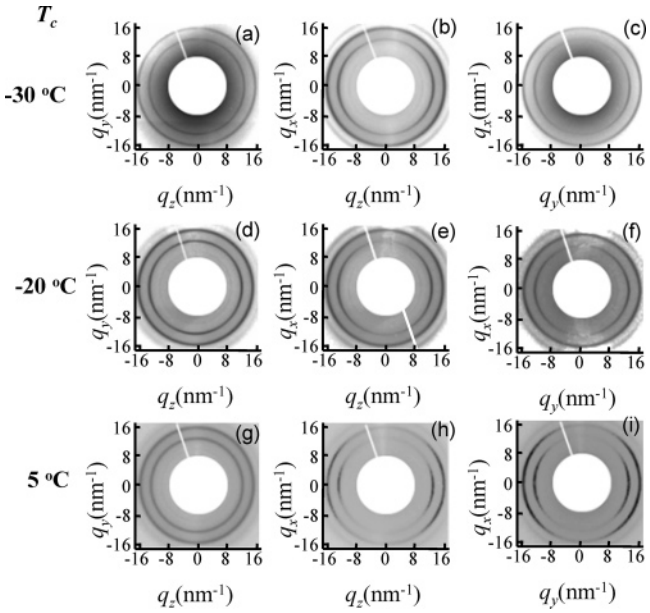

Figure 5. Sets of 2D WAXS patterns of PEO-*b*-PS in the T_x region with the PEO crystals' *c*-axes parallel to the cylinder axis direction. (a) T_x = −30 °C when the X-ray beam is along the *x* direction; (b) T_x = −30 °C when the X-ray beam is along the *y* direction; (c) T_x = −30 °C when the X-ray beam is along the *z* direction; (d) T_x = −20 °C when the X-ray beam is along the *x* direction; (e) T_x = −20 °C when the X-ray beam is along the *y* direction; (f) T_x = −20 °C when the X-ray beam is along the *z* direction; (g) T_x = 5 °C when the X-ray beam is along the *x* direction; (h) T_x = 5 °C when the X-ray beam is along the *y* direction; and (i) T_x = 5 °C when the X-ray beam is along the *z* direction.

crystal orientation in this T_x region in the IHC confinement can be schematically drawn and is shown in Figure 6b (the top view along the *x* direction of the IHC phase.) A cross-section view along the OO′ line is attached at the bottom of this figure. In this figure, the *c*-axes of the PEO crystals are parallel to the *x* direction and the *b*-axes are randomly oriented in the *yz* plane. It is thus expected that the 2D WAXS patterns should be identical to the fiber pattern of PEO crystals when the X-ray is along the *y* and *z* directions.[55] As evidenced by the broad (120) diffraction arcs on the equator in these figures, the PEO crystals studied here are less oriented when they are compared with those 2D WAXS patterns observed in the confined lamellar and HPL structures with the same crystal orientations (fiber pattern).[23,26,27,32]

The observation of this crystal orientation is surprising to us because our previous studies of the PEO crystal orientation changes in the HC phase (the PS formed the matrix and PEO formed the cylinders) show that the *c*-axes of PEO crystals were not observed to be parallel to $\hat{a}$ in the entire T_x region studied.[26,32] We speculate that the confinement size (the diameter of the PEO cylinder) in the HC phase structure is smaller (less than 14 nm)[26,32] than that in the IHC phase. (The upper limit of the in-plane lateral sizes for the PEO blocks is estimated to be

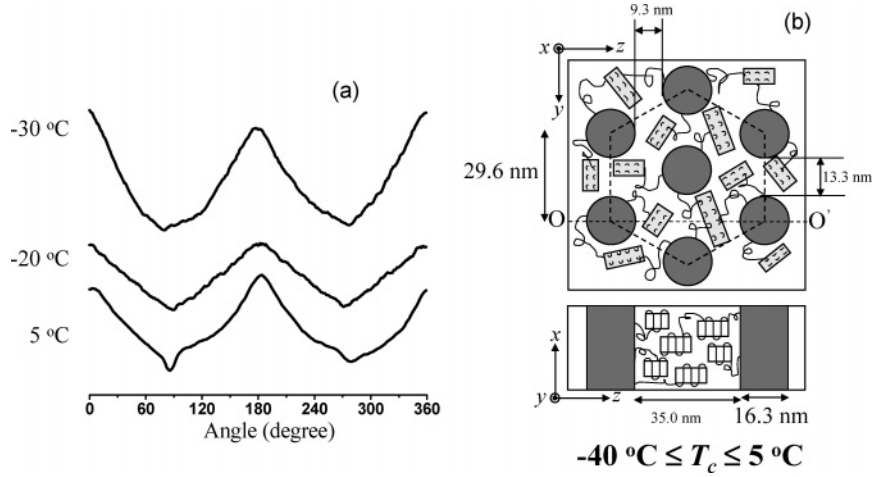

Figure 6. Azimuthal profiles of the (120) reflections on the first ring when $T_x = -30$, -20, and 5 °C, when the X-ray beam is along the *y* direction (a); a schematic drawing of a *c*-axis orientation in PEO crystals parallel to $\hat{a}$ crystallized outside of the PS cylinders (b).

Table 1. Long Period *L*, Weight Percentage Crystallinity w_c, Volume Percentage Crystallinity v_c, and Lamellar Thickness *l* of PEO Crystals when Crystallized between −30 and 5 °C

T_x (°C)	−30	−20	−10	0	5
L (nm)[a]	14.4	14.2	14.3	13.9	14.0
w_c[b]	0.637	0.639	0.637	0.648	0.650
v_c[c]	0.614	0.616	0.614	0.625	0.628
l (nm)[d]	8.8	8.7	8.8	8.7	8.8

[a] Long period of PEO amorphous and crystals. [b] PEO weight percentage crystallinities, obtained in DSC experiments. [c] PEO volume percentage crystallinities, $v_c = \rho_a w_c/[\rho_a w_c + \rho_c (1 - w_c)]$, where ρ_c and ρ_a are the density of crystalline and amorphous PEO, respectively. At room temperature, $\rho_c = 1.239$ g/cm^3 and $\rho_a = 1.124$ g/cm^3. [d] PEO crystal lamellar thickness, $l = Lv_c$.

35.0 nm; see the bottom view in Figure 6b.) Furthermore, the difference of the tethered PEO blocks on a convex or a concave PS solid surface may also affect the PEO block crystallization and crystal orientation. Note that in the other two studies for crystallization in the IHC phase this *c*-axis orientation has also not been reported.[13,14]

Additional structural information can also be obtained by careful examinations of the 2D SAXS patterns in Figure 3b,c at $T_x = -20$ °C. In these figures, a pair of the scattering arcs on the meridian direction (along $\hat{a}$, the *x* direction) can be observed. After examining each 2D SAXS pattern obtained in this T_x region (-30 °C $\le T_x \le$ 5 °C), all of them show the similar scattering arcs located along the *x* direction, as shown in Figure 3b,c. These scattering arcs result from the long period, *L*, of the PEO block crystals due to the parallel orientation of the *c*-axes of the PEO crystals and $\hat{a}$ in this T_x region.[29] When the $T_x >$ 5 °C, those scattering arcs cannot be observed in the 2D SAXS patterns because of the change of the PEO crystal orientations (see below). The *L* values are between 13.0 and 14.4 nm within this T_x region. Since the DSC results show that the weight crystallinity of PEO is ~65% when the sample was crystallized between −30 and 5 °C, the thickness of PEO crystals within this temperature range can be roughly calculated using the model previously developed.[29] The lamellar thicknesses of the PEO crystals, *l*, at different T_x values are in the vicinity of 8.7−8.8 nm. They are also included in Table 1.

Crystal Orientation When Crystallized between 10 °C ≤ T_x ≤ 20 °C. Figure 7 shows two sets of 2D WAXS patterns of a sheared PEO-*b*-PS sample when the X-ray beam is aligned along the *x*, *y*, and *z* directions after the sample is crystallized at $T_x =$ 10 and 20 °C, respectively. The 2D WAXS patterns in Figure 7a,d (when the X-ray beam is along the *x* direction) are again

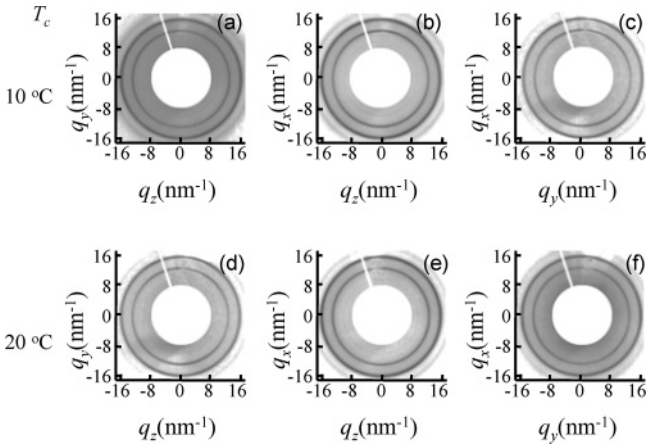

Figure 7. Sets of 2D WAXS patterns of PEO-*b*-PS in the T_x region with the PEO crystals' *c*-axes tilted to the cylinder axis direction. (a) $T_x = 10$ °C, the X-ray beam was along the *x* direction; (b) $T_x = 10$ °C, the X-ray beam was along the *y* direction; (c) $T_x = 10$ °C, the X-ray beam was along the *z* direction; (d) $T_x = 20$ °C, the X-ray beam was along the *x* direction; (e) $T_x = 20$ °C, the X-ray beam was along the *y* direction; and (f) $T_x = 20$ °C, the X-ray beam was along the *z* direction.

isotropic. When the X-ray beam is aligned along the *y* and *z* directions, Figure 7b,c,e,f exhibits that the (120) diffraction maxima are located in the quadrants. Figure 8a shows two azimuthal scanning profiles for those (120) diffractions at these two T_x values. Four maxima in each of the azimuthal scanning profiles can be observed. This reveals that a specifically preferred crystal orientation of the *c*-axes of the PEO crystals exists and is inclined with respect to $\hat{a}$. Furthermore, with increasing T_x, the tilting angle increases from 47° at 10 °C to 70°at $T_x = 20$ °C (angle is from the *c*-axis toward the direction which is perpendicular to $\hat{a}$). A real space model for the PEO crystal orientation between 10 °C $\le T_x \le$ 20 °C in the IHC confinement is schematically drawn and shown in Figure 8b. From the top view of the IHC structure (along the *x* direction), the PEO crystals are randomly oriented along the *x* direction, while from the cross-section view in the bottom of this figure, the *c*-axes of PEO crystals are tilted with respect to $\hat{a}$.

Figure 9 shows the change of the angle between the *c*-axes of PEO crystals and $\hat{a}$ with T_x values, which is different from the observation in both the HC phase and HPL phase confinements.[26−28,32] Note that the tilt angle change with T_x values are close to identical for these three sheared samples independently prepared with a deviation of ±5°. In fact, if Figure

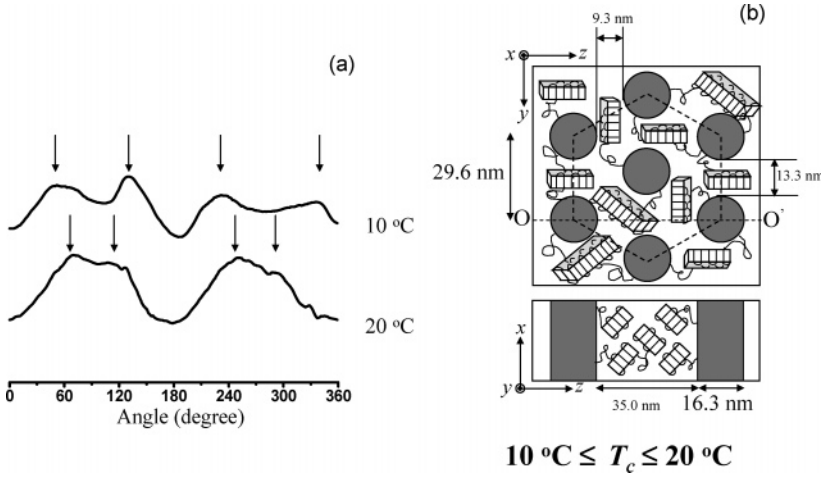

Figure 8. Azimuthal profiles of the (120) reflections on the first ring when T_x = 10 and 20 °C, when the X-ray is along the *y* direction (a); a schematic drawing of a *tilted* crystal orientation confined outside of the PS cylinders (b).

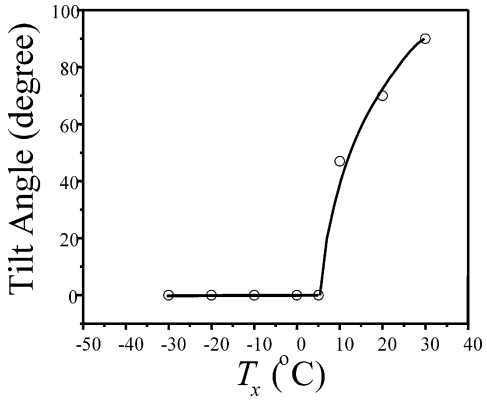

Figure 9. Changes of the angle between the *c*-axis of the PEO crystals and $\hat{a}$ at different T_x values. The deviation for each data point in three sheared samples independently prepared is ±5°.

8b is a true representation of the PEO crystal orientation, we should also observe a pair of the (120) diffractions on the equator in the 2D SAXS patterns. In our observations, the pair of diffractions may be buried in the smeared scattering of the azimuthal scanning profiles. This implies that the *c*-axes of the PEO crystals are not as oriented as those in the HC confinement due to the fact that the confinement sizes in the IHC phase are less uniform within the *yz* plane compared to the confinement size (diameter of the PEO cylinder) in the HC phase. The tilting angle may also be sensitive to the confinement sizes.[29]

Crystal Orientation When Crystallized at 30 °C. Parts a, b, and c of Figure 10 show a set of 2D WAXS patterns of a mechanically sheared sample crystallized at T_x = 30 °C when the X-ray beam is aligned along the *x*, *y*, and *z* directions. It is particularly interesting that in Figure 10a the 2D WAXS pattern taken along the *x* direction shows three (120) diffraction pairs with a 6-fold hexagonal symmetry. The azimuthal scanning profile X in Figure 11a represents the (120) diffractions in the WAXS pattern of Figure 10a. The six maxima are observed at around ϕ = 30°, 90°, 150°, 210°, 270°, and 330°, indicating that the PEO crystals preferentially orient into three directions that are 120° apart from each other. Comparing this 6-fold symmetry in the WAXS patterns with the 2D SAXS pattern of the IHC phase structure (see Figure 3a), we can deduce that the PEO crystal growth is guided along the $\{10\bar{1}0\}$ planes of the hexagonal PS cylinder lattice. Namely, the *c*-axes of the PEO crystals are parallel to the $\{1\bar{2}10\}$ planes.

This result is similar to the observed PEO crystal orientation in the HPL phase where the PEO crystals are along the $\{10\bar{1}0\}$ planes of the hexagonal perforated PS cylinders.[27,28] However, it differs from the PE crystal orientation observed in the IHC phase morphology of the PVCH-*b*-PE copolymer, where the *c*-axes of the PE crystals is parallel to the $\{10\bar{1}0\}$ planes of the IHC phase.[14] Possible reasons for this difference may result from the different crystal growth direction in these two different crystal structures of PEO and PE (PEO growth along the [120] in the monoclinic unit cell and PE growth along the *b*-axis in the orthorhombic unit cell). More importantly, the chain direction in the PE crystals is tilted with respect to the *b*-axis at an angle from 18° to 35° usually but up to 45° at high T_x values.[56]

In Figure 10b,c, 2D WAXS patterns where the X-ray beam is aligned along the *y* and *z* directions show the (120) reflections located on the meridian, indicating that the *c*-axes of the PEO crystals are oriented perpendicular to $\hat{a}$. These patterns can be explained using a [120] uniaxial pattern.[23] The azimuthal scanning profiles Y and Z in Figure 11a represent the (120) diffractions when the X-ray beam is along the *y* and *z* directions. Two major maxima appear at 90° and 270°, indicating that they are on the meridian. However, there are also shoulders near the meridian. They may result from some minor population of the *c*-axes of the PEO crystals that are still tilted with respect to the â-axis and/or some PEO amorphous halos may be oriented in those azimuthal angle regions. This *c*-axis orientation of the PEO crystals at T_x = 30 °C is identical to the PEO crystal orientation in the confined HC phase[26,32] but different from that in the confined HPL phase. In the HPL phase, the *c*-axis orientation of the PEO crystals is determined by a combination of both the preference of the PEO blocks tethered on the PS layers and the perforated PS cylinders in the confined sizes.[27,28]

In the ideal case of a monodomain IHC phase where the PEO blocks are crystallized outside of the PS cylinders, the 2D WAXS patterns obtained when the X-ray beam is aligned along the *y* and *z* directions should not be identical since the X-ray beam is parallel and perpendicular to the $\{10\bar{1}0\}$ plane of the IHC phase, respectively. A real space model for the PEO crystal orientation crystallized at 30 °C in the IHC confinement is schematically drawn in Figure 11b, in which the *c*-axes of the PEO crystals are perpendicular to $\hat{a}$. If one views from the top of the IHC phase (along the *x* direction), the PEO lamellar crystals preferentially grow along the $\{10\bar{1}0\}$ planes of the PS cylinders in the IHC phase at this T_x. Therefore, when the X-ray beam is aligned along the *y* direction, there should be only one pair of (120) diffractions appearing on the meridian and no (120)

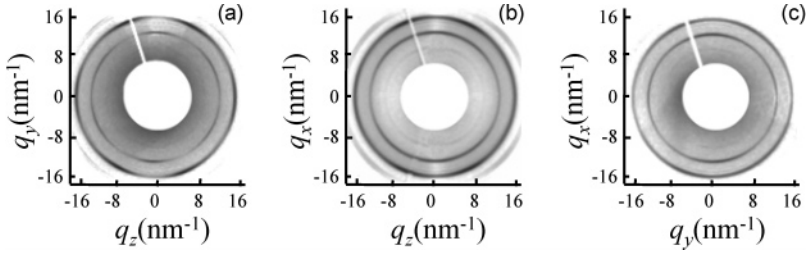

Figure 10. Set of 2D WAXS patterns of PEO-*b*-PS in the T_x region with the PEO crystals' *c*-axes perpendicular to the cylinder axis direction: (a) $T_x = 30$ °C when the X-ray beam was along the *x* direction; (b) $T_x = 30$ °C when the X-ray beam was along the *y* direction; and (c) $T_x = 30$ °C when the X-ray beam was along the *z* direction.

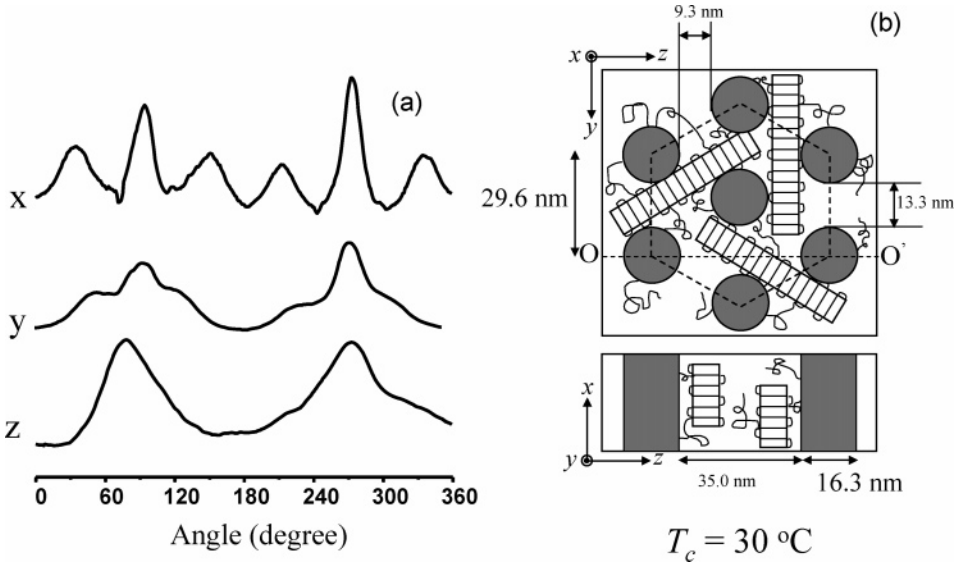

Figure 11. Azimuthal profiles of the (120) reflections on the first ring when $T_x = 30$ °C; curves X, Y, and Z represent the results when the X-ray is along the *x*, *y*, and *z* directions, respectively (a). Schematic drawings of PEO crystals with a *c*-axis orientation perpendicular to â outside of the PS cylinders (b).

observed on the equator. On the other hand, when the X-ray beam is along the *z* direction, the (120) diffraction should be on both the meridian and equator. Since we do not have a perfect monodomain structure of the IHC phase as illustrated in Figure 3a−c, no obvious difference in both of the 2D WAXS patterns can be found as is shown in the azimuthal scanning profiles Y and Z in Figure 11a.

The reason for the PEO crystal adopting the [120] growth direction along the $\{10\bar{1}0\}$ planes must be attributed to lower nucleation densities (thus, larger sizes) of the PEO crystals which can grow a longer distance than the restriction imposed by the PS cylinders before the impingement with other PEO crystals. In this case, as shown in Figure 11b, one [120] direction in the PEO crystals is directed along the $\hat{a}$ direction, and the other growth direction is along the $\{10\bar{1}0\}$ planes, namely, along the $[1\bar{2}10]$ direction of the hexagonal PS cylinders. The PEO lamellar crystal thickness is controlled by the distance between the neighboring PS cylinders along the $[10\bar{1}0]$ direction, which can be calculated to be 9.3 nm (see Figure 11b). Although this lamellar crystal thickness is limited, the *c*-axis orientation of the PEO crystals provides the maximum crystallinity development with a low primary nucleation density.

Apparent Crystallite Size Estimations Using the Scherrer Equation. In order to study the shape and size of the PEO crystals within the IHC phase, we perform data analysis of the (120) diffractions from the WAXS patterns along the *y* direction by using the Scherrer equation. The definitions of the (120) crystallite sizes are as follows. In the T_x region between −30 and 5 °C, the *c*-axes of the PEO crystals are parallel to $\hat{a}$. Two

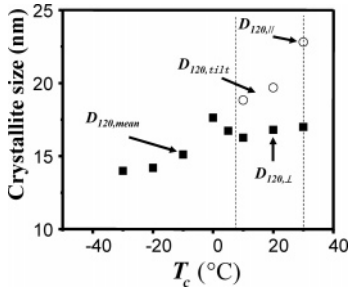

Figure 12. Apparent crystallite size analysis for the (120) diffractions at different T_x values in the 2D WAXS patterns when X-ray beam is along the *y* direction.

sets of (120) diffraction pairs are both located on the equator in the 2D WAXS patterns. Therefore, only one mean (120) crystallite size can be obtained in this T_x region, $D_{120,mean}$. Above $T_x = 5$ °C the *c*-axes of the PEO crystals start to tilt with respect to $\hat{a}$. We can have two (120) crystallite sizes: one represents the (120) direction perpendicular to $\hat{a}$, ($D_{120,\perp}$), and another is the (120) direction tilt (10 °C ≤ T_x ≤ 20 °C) to $\hat{a}$, $D_{120,tilt}$. Finally, at $T_x = 30$ °C, the *c*-axis of PEO crystals is perpendicular to $\hat{a}$. Two (120) crystallite sizes can be identified: $D_{120,\perp}$ and $D_{120,\parallel}$.

Figure 12 shows the calculated (120) lateral crystallite sizes at different T_x values for the mechanically sheared sample. Between −30 °C ≤ T_x ≤ 5 °C, the $D_{120,mean}$ value gradually and slightly increases with increasing T_x and reaches a maximum when $T_x = 0$ °C. The value of this maximum is 17.6 nm, which is smaller than the upper limit of the distance between two PS

cylinders in the lateral direction, 35.0 nm. Although the calculated $D_{120,mean}$ reflects merely a lower limit of the actual crystal size, the values of the $D_{120,mean}$ between $-30\ °C \leq T_x \leq 5\ °C$ in Figure 12 are consistent with our conclusion that the PEO crystals are "confined" outside of the hexagonal PS cylinders. We speculate that one of the reasons for the maximum value of $D_{120,mean}$ at 0 °C may be associated with a change in the nucleation type from homogeneous to heterogeneous nucleation. It was reported that the homogeneous to heterogeneous nucleation change for a PEO having an M_n of about 10K g/mol occurred at a T_x around 0 °C.[57]

Figure 12 also shows the apparent crystallite sizes along two perpendicular directions, the $D_{120,\perp}$ and $D_{120,tilt}$, when $10\ °C \leq T_x \leq 20\ °C$. It has been found that $D_{120,tilt} > D_{120,\perp}$ since the confinement along the $D_{120,tilt}$ direction is gradually released when the tilting angle increases. In this range of the apparent crystallite sizes, it seems that they still represent the true PEO crystal dimensions. At $T_x = 30\ °C$, the PEO crystal growth along the $D_{120,\perp}$ direction, which is parallel to $\hat{a}$, is limited by both the restrictions of the PS cylinders and the impingement of neighboring crystals along the $\hat{a}$ direction. On the other hand, the PEO crystal growth along the $D_{120,||}$ direction is only limited by the impingement of the neighboring crystals. At this T_x, the true PEO crystal dimensions may exceed the calculated $D_{120,||}$ apparent crystallite sizes.

Conclusion

In summary, the IHC phase in the PEO-*b*-PS diblock copolymer has been identified by SAXS experiments. The T_x-dependent crystal orientations are studied by using combined 2D SAXS and WAXS techniques in this "confined" IHC phase morphology. Four T_x regions are recognized for different crystal orientations. Namely, the *c*-axes in the PEO crystals are randomly oriented in the HPL structure when $T_x < -40\ °C$, which is achieved by directly quenching the sample into liquid nitrogen. The *c*-axes in the PEO crystals are preferentially oriented parallel to $\hat{a}$ of the IHC structure between $-30\ °C \leq T_x \leq 5\ °C$. With increasing T_x to the region between 10 and 20 °C, the *c*-axes in the PEO crystals are preferentially oriented at an incline to $\hat{a}$ of the IHC phase. The tilt angle of the *c*-axis with respect to the cylinder axis increases with increasing T_x. Perpendicular crystal orientation of the *c*-axis with respect to $\hat{a}$ is observed in this IHC confinement when T_x reaches 30 °C. When $T_x < 30\ °C$, the PEO crystals are "confined" in the hexagonal compartments of the PS cylinders due to the higher nucleation densities. At $T_x = 30\ °C$, the PEO lamellar crystals are tailored to grow along the $\{10\bar{1}0\}$ planes of the IHC lattice because of a lower nucleation density. This PEO block crystal orientation change in the IHC phase is clearly different from those in the HC phase and HPL phase nanoconfined environments.

Acknowledgment. This work was supported by NSF (DMR-0516602). The 2D SAXS and WAXS research was carried out at the National Synchrotron Light Source in Brookhaven National Laboratory supported by the Department of Energy. We appreciate the set up of a Pyris Diamond DSC by the Perkin-Elmer Co. in SZDC's laboratory.

References and Notes

(1) Séguéla, R.; Prud'homme, J. *Polymer* **1989**, *30*, 1446.
(2) Cohen, R. E.; Cheng, P. L.; Douzinas, K. C.; Kofinas, P.; Berney, C. V. *Macromolecules* **1990**, *23*, 324.
(3) Douzinas, K. C.; Cohen, R. E. *Macromolecules* **1992**, *25*, 5030.
(4) Sakurai, K.; MacKnight, W. J.; Lohse, D. J.; Schulz, D. N.; Sissano, J. A. *Macromolecules* **1993**, *26*, 3236.
(5) Cohen, R. E.; Bellare, A.; Drzewinski, M. A. *Macromolecules* **1994**, *27*, 2321.
(6) Khandpur, A. K.; Macosko, C. W.; Bates, F. S. *J. Polym. Sci., Polym. Phys. Ed.* **1995**, *33*, 247.
(7) Hamley, I. W.; Fairclough, J. P. A.; Ryan, A. J.; Bates, F. S.; Towns-Andrews, E. *Polymer* **1996**, *37*, 4425.
(8) Hamley, I. W.; Fairclough, J. P. A.; Terrill, N. J.; Ryan, A. J.; Lipic, P. M.; Bates, F. S.; Towns-Andrews, E. *Macromolecules* **1996**, *29*, 8835.
(9) Zhao, J.; Majumdar, B.; Schulz, M. F.; Bates, F. S.; Almdal, K.; Mortensen, K.; Hajduk, D. A.; Gruner, S. M. *Macromolecules* **1996**, *29*, 1204.
(10) Quiram, D. J.; Register, R. A.; Marchand, G. R. *Macromolecules* **1997**, *30*, 4551.
(11) Quiram, D. J.; Register, R. A.; Marchand, G. R.; Adamson, D. H. *Macromolecules* **1998**, *31*, 4891.
(12) Weimann, P. A.; Hajduk, D. A.; Chu, C.; Chaffin, K. A.; Brodil, J. C.; Bates, F. S. *J. Polym. Sci., Polym. Phys.* **1999**, *37*, 2053.
(13) Park, C.; De Rosa, C.; Fetters, L. J.; Thomas, E. L. *Macromolecules* **2000**, *33*, 7931.
(14) Loo, Y. L.; Register, R. A.; Adamson, D. H. *Macromolecules* **2000**, *33*, 8361.
(15) Loo, Y. L.; Register, R. A.; Ryan, A. J.; Dee, G. T. *Macromolecules* **2001**, *34*, 8968.
(16) Loo, Y. L.; Register, R. A.; Ryan, A. J. *Macromolecules* **2002**, *35*, 2365.
(17) Takeshita, H.; Ishii, N.; Araki, C.; Miya, M.; Takenaka, K.; Shiomi, T. *J. Polym. Sci., Polym. Phys. Ed.* **2004**, *42*, 4199.
(18) Hirata, E.; Ijitsu, T.; Hashimoto, T.; Kawai, H. *Polymer* **1975**, *16*, 249.
(19) Yang, Y. W.; Tanodekaew, S.; Mai, S. M.; Booth, C.; Ryan, A. J.; Bras, W.; Viras, K. *Macromolecules* **1995**, *28*, 6029.
(20) Hillmyer, M. A.; Bates, F. S. *Macromol. Symp.* **1997**, *117*, 121.
(21) Hamley, I. W.; Wallwork, M. L.; Smith, D. A.; Fairclough, J. P. A.; Ryan, A. J.; Mai, S. M.; Yang, Y. W.; Booth, C. *Polymer* **1998**, *39*, 3321.
(22) Zhu, L.; Chen, Y.; Zhang, A.; Calhoun, B. H.; Chun, M.; Quirk, R. P.; Cheng, S. Z. D.; Thomas, E. L.; Hsiao, B. S.; Yeh, F.; Hashimoto, T. *Phys. Rev. B* **1999**, *60*, 10022.
(23) Zhu, L.; Cheng, S. Z. D.; Calhoun, B. H.; Ge, Q.; Quirk, R. P.; Thomas, E. L.; Hsiao, B. S.; Yeh, F.; Lotz, B. *J. Am. Chem. Soc.* **2000**, *122*, 5957.
(24) Zhu, L.; Cheng, S. Z. D.; Calhoun, B. H.; Ge, Q.; Quirk, R. P.; Thomas, E. L.; Hsiao, B. S.; Yeh, F.; Lotz, B. *Polymer* **2001**, *42*, 5829.
(25) Zhu, L.; Mimnaugh, B. R.; Ge, Q.; Quirk, R. P.; Cheng, S. Z. D.; Thomas, E. L.; Lotz, B.; Hsiao, B. S.; Yeh, F.; Liu. L. *Polymer* **2001**, *42*, 9121.
(26) Huang, P.; Zhu, L.; Cheng, S. Z. D.; Ge, Q.; Quirk, R. P.; Thomas, E. L.; Lotz, B.; Hsiao, B. S.; Liu, L.; Yeh, F. *Macromolecules* **2001**, *34*, 6649.
(27) Zhu, L.; Huang, P.; Chen, W. Y.; Ge, Q.; Quirk, R. P.; Cheng, S. Z. D.; Thomas, E. L.; Lotz, B.; Hsiao, B. S.; Yeh, F.; Liu, L. *Macromolecules* **2002**, *35*, 3553.
(28) Zhu, L.; Cheng, S. Z. D.; Huang, P.; Ge, Q.; Quirk, R. P.; Thomas, E. L.; Lotz, B.; Hsiao, B. S.; Yeh, F.; Liu, L. *Adv. Mater.* **2002**, *14*, 31.
(29) Huang, P.; Zhu, L.; Guo, Y.; Ge, Q.; Jing, A. J.; Chen, W. Y.; Quirk, R. P.; Cheng, S. Z. D.; Thomas, E. L.; Lotz, B.; Hsiao, B. S.; Avila-Orta, C. A.; Sics, I. *Macromolecules* **2004**, *37*, 3689.
(30) Vasilev, C.; Heinzelmann, H.; Reiter, G. *J. Polym. Sci., Polym. Phys. Ed.* **2004**, *42*, 1312.
(31) Xu, J. T.; Xue, L.; Mai, S. M.; Ryan, A. J. *J. Appl. Polym. Sci.* **2004**, *93*, 870.
(32) Huang, P.; Guo, Y.; Quirk, R. P.; Ruan, J.; Lotz, B.; Thomas, E. L.; Hsiao, B. S.; Avila-Orta, C. A.; Sics, I.; Cheng, S. Z. D. *Polymer* **2006**, *47*, 5457.
(33) Ho, R.-M.; Lin, F.-H.; Tsai, C.-C.; Lin, C.-C.; Ko, B.-T.; Hsiao, B. S.; Sics, I. *Macromolecules* **2004**, *37*, 5985.
(34) Fu, J.; Luan, B.; Pan, C.; Li, B.; Han, Y. *Macromolecules* **2005**, *38*, 5118.
(35) Jia, L.; Yin, L.; Li, Y.; Li, Q.; Yang, J.; Yu, J.; Shi, Z.; Fang, Q.; Cao, A. *Macromol. Biosci.* **2005**, *5*, 526.
(36) Nojima, S.; Yamamoto, S.; Ashida, T. *Polym. J.* **1995**, *27*, 673.
(37) Nojima, S.; Kato, K.; Yamamoto, S.; Ashida, T. *Macromolecules* **1992**, *25*, 2237.
(38) Ho, R.-M.; Chiang, Y. W.; Lin, C. C.; Huang, B. H. *Macromolecules* **2005**, *38*, 4769.
(39) Ishikawa, S.; Ishizu, K.; Fukotomi, T. *Polym. Commun.* **1991**, *32*, 374.
(40) Liu, L.-Z.; Yeh, F.; Chu, B. *Macromolecules* **1996**, *29*, 5335.
(41) Liu, L.-Z.; Chu, B. *J. Polym. Sci., Polym. Phys. Ed.* **1999**, *37*, 779.

(42) Mortensen, K.; Brown, W.; Almdal, K.; Alami, E.; Jada, A. *Langmuir* **1997**, *13*, 3635.
(43) Quiram, D. J.; Register, R. A.; Marchand, G. R.; Ryan, A. J. *Macromolecules* **1997**, *30*, 8338.
(44) Xu, J.-T.; Fairclough, J. P. A.; Mai, S.-M.; Ryan, A. J.; Chaibundit, C. *Macromolecules* **2002**, *35*, 6937.
(45) Xu, J.-T.; Fairclough, J. P. A.; Mai, S.-M.; Chaibundit, C.; Mingvanish, M.; Booth, C.; Ryan, A. J. *Polymer* **2003**, *44*, 6843.
(46) Xu, J.-T.; Turner, S. C.; Fairclough, J. P. A.; Mai, S.-M.; Ryan, A. J.; Chaibundit, C.; Booth, C. *Macromolecules* **2002**, *35*, 3614.
(47) Chaibundit, C.; Mingvanish, W.; Booth, C.; Mai, S.-M.; Turner, S. C.; Fairclough, J. P. A.; Ryan, A. J.; Pissis, P. *Macromolecules* **2002**, *35*, 4838.
(48) Viras, K.; Kelarakis, A.; Havredaki, V.; Mai, S.-M.; Ryan, A. J.; Mistry, D.; Mingvanish, W.; MacKenzie, P.; Booth, C. *J. Phys. Chem.* **2003**, *107*, 6946.
(49) Ruokolainen, J.; Mezzenga, R.; Fredrickson, G. H.; Kramer, E. J.; Hustad, P. D.; Coates, G. W. *Macromolecules* **2005**, *38*, 851.
(50) Chen, E.; Xia, Y.; Graham, M. J.; Foster, M. D.; Mi, Y.; Wu, W.; Cheng, S. Z. D. *Chem. Mater.* **2003**, *15*, 2129.
(51) Lu, Z.-H.; Krause, S. *Macromolecules* **1982**, *15*, 112.
(52) Quirk, R. P.; Kim, J.; Kausch, C.; Chun, M. S. *Polym. Int.* **1996**, *39*, 3.
(53) Alexander, L. E. *X-ray Diffraction Methods in Polymer Science*; Wiley-Interscience: New York, 1969.
(54) Lee, S.; Miyaji, H.; Geil, P. H. *J. Macromol. Sci., Phys.* **1983**, *B22*, 489.
(55) Takahashi, Y.; Tadokoro, H. *Macromolecules* **1973**, *6*, 672.
(56) Lotz, B.; Cheng, S. Z. D. *Polymer* **2005**, *46*, 577 and references cited in this article.
(57) Koutsky, J. A.; Walton, A. G.; Baer, E. *J. Appl. Phys.* **1967**, *38*, 1832.

MA061871H